Large-Scale Simulations of a Non-generic Helicopter Engine Nozzle and a Ducted Axial Fan

Mehmet Onur Cetin, Alexej Pogorelov, Andreas Lintermann, Hsun-Jen Cheng, Matthias Meinke, and Wolfgang Schröder

Abstract Large-eddy simulations (LESs) of a helicopter engine jet and an axial fan are performed by using locally refined Cartesian hierarchical meshes. For the computations a high-fidelity, massively parallelized solver for compressible flow is used. To verify the numerical method, a coaxial hot round jet is computed and the results are compared to reference data. The analysis is complemented by a grid convergence study for both applications, i.e., for the helicopter engine jet and the axial fan. For the helicopter engine jet, additional computations have been performed for two different nozzle geometries, i.e., a simplified nozzle geometry that is consisting of a center body and divergent outer annular channel, and a complete engine nozzle geometry with four additional struts were used. The presence of the struts results in a different potential core break-down and turbulence intensity. Furthermore, for the axial fan configuration, computations have been performed at two different volume flow rates. The reduction of the volume flow rate results in an interaction of the tip-gap vortex with the neighboring blade which leads to a higher turbulent kinetic energy near and inside the tip-gap region.

1 Introduction

The prediction and reduction of noise generated by turbulent flows has become one of the major tasks of todays aircraft development and is also one of the key goals in European aircraft policy. Compared to the year 2000 the perceived noise level of flying aircraft should to be reduced by 65 % until the year 2050. To comply with

M.O. Cetin (✉) • A. Pogorelov • A. Lintermann • H.J. Cheng
Institute of Aerodynamics, RWTH Aachen University, Wüllnerstr. 5a, 52062 Aachen, Germany
e-mail: office@aia.rwth-aachen.de

M. Meinke • W. Schröder
Institute of Aerodynamics, RWTH Aachen University, Wüllnerstr. 5a, 52062 Aachen, Germany

Forschungszentrum Jülich, 52425 Jülich, Germany

JARA – High-Performance Computing, 52062 Aachen, Germany
e-mail: office@aia.rwth-aachen.de

new noise level regulations, reliable, efficient and accurate aeroacoustic predictions are required, i.e., for low noise design of technical devices such as helicopter engine nozzles or axial fans.

In jet and fan flows as investigated in this paper, the acoustic field is dependent on the unsteady turbulent flow field. That is, the reliability of the acoustic field prediction is strictly related to the accuracy of the flow field solution. However, the accurate prediction of the turbulent flow field requires extensive computing resources, i.e., the solution of the turbulent flow field necessitates a scale resolving LES that requires a high mesh resolution to cover the major part of the turbulence energy spectrum.

Codes used in industry mainly rely on computationally efficient solutions of the Reynolds averaged Navier-Stokes equations (RANS), they, however, only provide solutions which are time averaged over all turbulent scales. In contrast, details of the turbulent flow field obtained by an LES allow a thorough analysis of the physical mechanisms responsible for the noise generation and therefore provide valuable information for design modifications resulting in reduced noise emission.

With the recent substantial growth of the computing technology, numerical simulation methods such as LES is possible for the flow field prediction of many simplified practical applications. Vast number of studies have been done in the past to numerically simulate for instance, jets with simplified nozzle geometries under laboratory conditions [1–3]. Moreover, few authors applied LES to tip leakage flows. Investigations have been performed, e.g., by You et al. [4–7] for a linear cascade with a moving end wall and Boudet et al. [8] for a single airfoil tip-clearance flow focusing on the noise generation. Real applications however, often have more complicated geometries and higher Reynolds numbers. Application-relevant Reynolds numbers, i.e., $Re > 10^5$ require large computational meshes. Additionally, the inclusion of geometries to the computational domain, e.g., a jet nozzle or an axial fan, requires additional local refinement of the mesh to avoid any unphysical flow behavior like boundary layer separations at the wall due to an underresolved turbulence spectrum. To overcome these difficulties and to analyze the grid dependence on the flow field, highly resolved LESs are performed in this study.

This paper is structured as follows. First, the numerical methods are presented in Sect. 2 and validated in Sect. 3. Subsequently, the results of nozzle-jet and axial fan simulations are discussed in Sects. 4 and 5. Computational features and scalability analysis are given in Sect. 6. Finally, some conclusion is outlined in Sect. 7.

2 Numerical Method

An LES model based on a finite volume method is used to simulate the compressible unsteady turbulent flow by solving the Navier-Stokes equations. For the LES an implicit grid filter is assumed and the monotone integrated LES (MILES) approach [9] is adopted, i.e., the dissipative part of the truncation error of the

numerical method is assumed to mimic the dissipation of the non-resolved subgrid scale stresses. This solution method has been validated and successfully used, e.g., in [10, 11]. The governing equations are spatially discretized by using the modified advection upstream splitting method (AUSM) [12]. The cell center gradients are computed using a second-order accurate least-squares reconstruction scheme [13], i.e., the overall spatial approximation is second-order accurate. For stability reasons, small cut-cells are treated using an interpolation and flux-redistribution method developed by Schneiders et al. [14]. A second order 5-stage Runge-Kutta method is used for the temporal integration. A massively parallel grid generator is used to create a computational hierarchical Cartesian mesh featuring local refinement [15]. The interested reader is referred to [12] for the details of the numerical methods, i.e., the discretization and computation of the viscid and inviscid fluxes.

3 Validation Test

To verify the solution procedure, a simulation of a coaxial hot round jet at a Mach number of $M = \frac{u_s}{a_s} = 0.9$ and a Reynolds number of $Re_D = \frac{\rho_s u_s D}{\mu} = 4 \times 10^5$ are performed, where u_s is the secondary jet inflow velocity, a_s is the sound speed, D is the jet diameter, ρ is the density and μ is the dynamic viscosity. The results are compared to the findings in [1]. A mesh with 24 million cells is used for the simulation. The computation and sampling time are chosen long enough to fulfill the statistical convergence, i.e., 5000 LES snapshots are used to average the flow field.

   To introduce turbulence, the jet is forced with artificial instability modes, that are introduced in the shear layers of the jet [16], where a hyperbolic tangential velocity profile is prescribed. The velocity distribution at the inlet section reads [1]

$$u_0(r) = \frac{u_s}{2}\left(1 + \tanh\frac{r_s - r}{2\delta_\theta}\right) + \frac{u_p - u_s}{2}\left(1 + \tanh\frac{r_p - r}{2\delta_\theta}\right). \tag{1}$$

where u_s is the secondary jet velocity, u_p is the primary jet velocity, r_s is the secondary jet radius, r_p is the primary jet radius and δ_θ is the momentum thickness which is chosen to be $0.05r_s$ [1]. The Inflow density distribution is defined by the Crocco-Buseman relation and the ideal gas law is used [1]. The flow parameters of the corresponding jet are shown in Table 1. Figure 1 illustrates the mean density contours and instantaneous vorticity field. To discuss the mean flow quantitatively, the streamwise profiles of the axial velocity and the jet half-width velocity are compared in Fig. 2. In agreement with the reference result, the velocity decay begins

Table 1 Simulation parameters (subscript 'p' is primary and 's' is secondary)

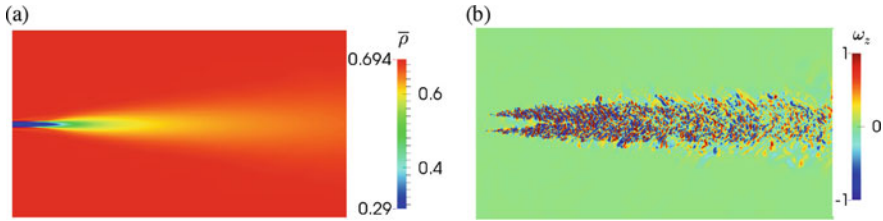| $Re = \rho_s u_s D/\mu_s$	$M = u_s/a_s$	u_s/u_p	T_s/T_∞	T_s/T_p	r_s/r_p
$400,000$	0.9	0.9	1.0	0.37	2

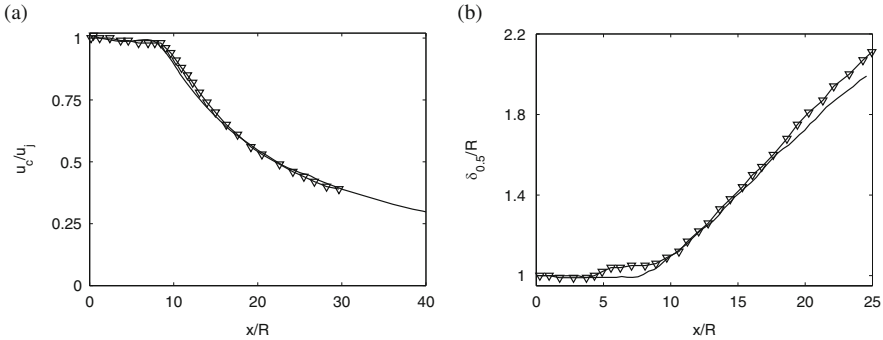Fig. 1 (a) Mean density contours, and (b) instantaneous vorticity contours

Fig. 2 Streamwise profiles of the, (a) axial velocity decay, and (b) jet half-width velocity for: (—) current simulation, (∇) Koh et al. [1]
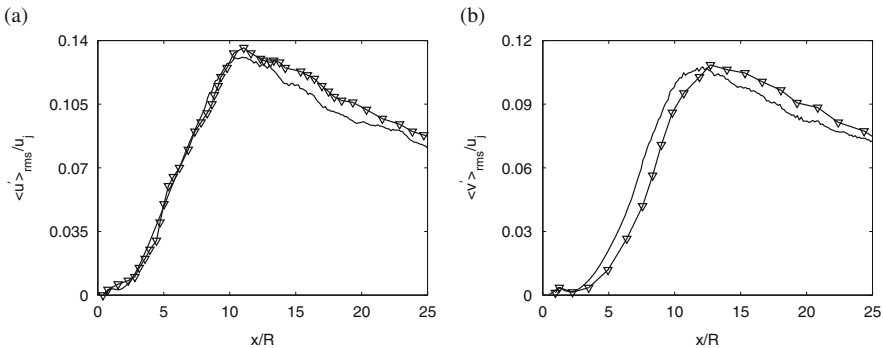

Fig. 3 Streamwise profiles of the, (a) rms fluctuating axial velocity, and (b) rms fluctuated radial velocity for: (—) current simulation, (∇) Koh et al. [1]

at the end of the potential core at about x $\approx$ 9R, where $R = D/2$ is the jet inlet radius in Fig. 2a. Moreover, as expected, the evolution of the jet half-width in Fig. 2b evidences a linear growth begins almost at the end of the potential core. The comparison shows a good agreement in the interval $0 < x/R < 18$. However, a slightly different jet spreading rate is observed for $x/R > 18$. Streamwise profiles of rms-axial and rms-radial velocity fluctuations are displayed in Fig. 3. Both profiles show

a good agreement with the reference data. A minor shift is detected on both profiles, where a slightly different potential core break down influences the Reynolds stress distribution of the jet. Overall, the comparisons of the first and second moment streamwise profiles show convincing agreement with the reference study.

4 Helicopter Engine Jet

In this section, simulation results of round jets emanating from a non-generic nozzle are presented. To investigate the grid dependence and influence of the nozzle geometry to the jet development two variants of the nozzle geometries are used. The Reynolds number is $Re_D = 7.5 \times 10^5$ based on the jet inlet diameter D, and the Mach number is M = 0.341.

4.1 Grid Convergence Test

The grid convergence study is done for two different meshes using the same geometry, i.e., case a and b. These meshes possess 0.329×10^9 and 1.097×10^9 cells, respectively. To ensure the statistical convergence 2250 LES snapshots for the case a and 3000 LES snapshots for the case b are used to average the flow field. A zoomed view on the mesh of case a is shown in Fig. 4. The computational specifications are given in Table 2. The nozzle geometry is included to the computational domain explicitly, where the inlet of the nozzle is located downstream of the last turbine stage.

Operating conditions are set at the inlet boundary that were taken from the measurements of a full-scale turbo-shaft engine [17]. Isotropic synthetic turbulence is injected at the inlet plane with approx. 10 % turbulence intensity [18]. For the outflow and lateral boundaries of the jet domain, static pressure is kept constant and other variables are extrapolated from the internal domain. To damp the numerical
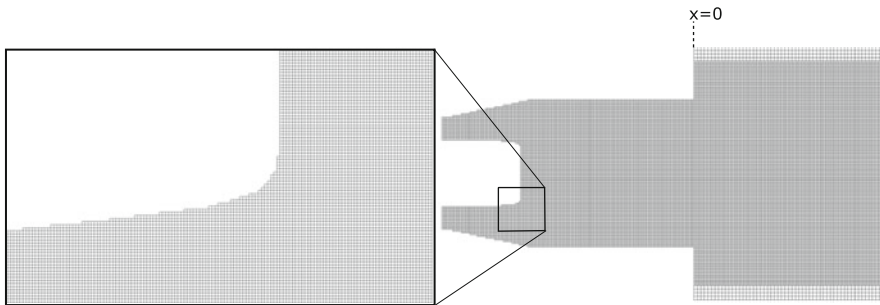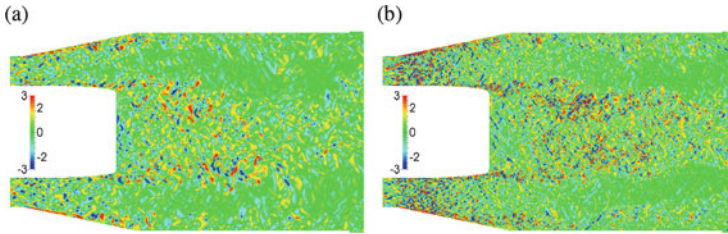

Fig. 4 Cartesian mesh view of the nozzle, *right*: resolution of a coarse mesh with 41 million cells, *left*: enlargement of a certain area for the case *a*

Table 2 Nozzle jet simulation parameters

	Re	M	Mesh cells	Simulation time
Jet case a	750, 000	0.341	329×10^6	480 D/u
Jet case b	750, 000	0.341	1097×10^6	440 D/u
Jet case c	750, 000	0.341	328×10^6	480 D/u

Fig. 5 Instantaneous axial velocity gradients in the rear part of the nozzle, (**a**) case a, (**b**) case b
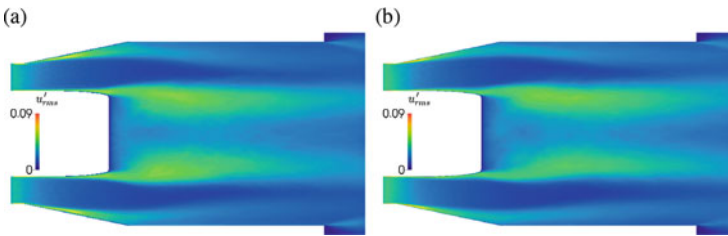
Fig. 6 Mean rms fluctuating axial velocity contours in the rear part of the nozzle, (**a**) case a, (**b**) case b

reflections at the boundaries, sponge layers are prescribed [19]. At the nozzle-wall a no-slip condition with a zero pressure and density gradient is applied.

The contours of the axial velocity gradients in streamwise direction are shown in Fig. 5. From the gradients distribution, it is obvious that the mesh resolution plays an important role in the formation of the turbulent structures in the rear part of the nozzle. To discuss the mean flow, a comparison based on the rms fluctuating axial velocity contours is displayed in Fig. 6. A juxtaposition of the centerline velocity decay is shown in Fig. 7a, where R is the nozzle-exit radius and u_j inflow velocity. An earlier potential core break-down is detected for the case b. However, downstream of the core, a similar velocity decay is observed.

Figure 7b illustrates the radial profile of the axial velocity at the nozzle-exit. The nozzle-exit profile is formed by the wake flow shedding from the center body, i.e., the velocity increases for $0 < r/R < 0.6$ and decreases for $r/R \geq 0.6$. Velocity profiles for case a and b are however, alike. At the nozzle wall however, a slight difference is observed due to the different boundary layer thicknesses. Streamwise
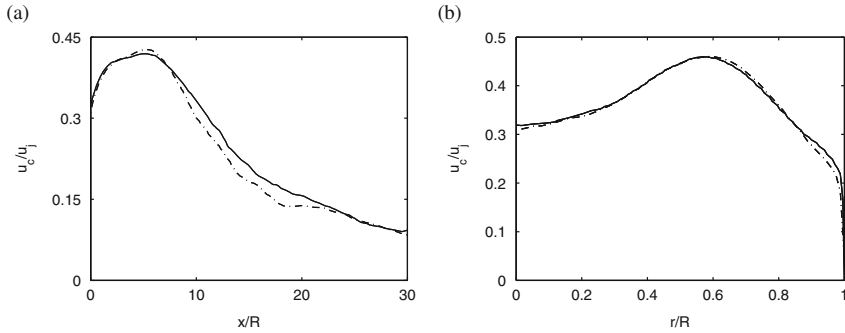
Fig. 7 (**a**) Streamwise profile of the mean centerline velocity, and (**b**) radial profile of the axial velocity at the nozzle-exit $x/R = 0$ for: (—) mesh case a, (-··-) mesh case b
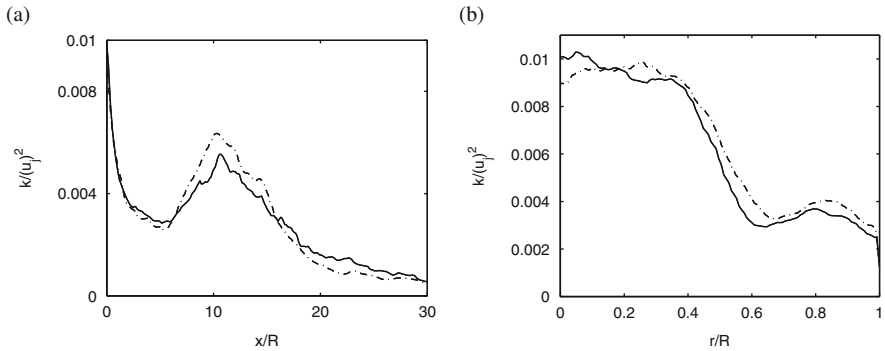

Fig. 8 (**a**) Streamwise profile of the turbulent kinetic energy, and (**b**) radial profile of the turbulent kinetic energy at the nozzle-exit $x/R = 0$ for: (—) case a, (-··-) case b

and radial profiles of the turbulent kinetic energy defined as

$$k = \frac{1}{2}\left(\overline{u'^2} + \overline{v'^2} + \overline{w'^2}\right). \tag{2}$$

are shown in Fig. 8. Both comparisons show that the behavior and the magnitude of the turbulent kinetic energy distribution almost coincides for both cases a and b. To summarize, from the grid dependence study it is obvious that a mesh resolution of $\mathcal{O}(300 \times 10^6)$ cells (case a), is fine enough to resolve important features of turbulence. This mesh resolution can therefore be regarded as sufficient.

4.2 Analysis of Two Variants of the Nozzle Geometry

In the following, two variants of the helicopter engine nozzle geometry are analyzed by simulation, i.e., first a simplified nozzle geometry (case *a*) which consist of a divergent annular nozzle and a center body, and a complete nozzle geometry (case *c*) with four additional struts which are supporting the center body inside the nozzle are used. A perspective view of the nozzle geometries is illustrated in Fig. 9. To visualize the turbulent jet flow field, the instantaneous 3D Q-criterion [20] of the jet of case *a* is illustrated in Fig. 10. The mean flow field is discussed in Fig. 11. The centerline velocity decay comparison in Fig. 11a evidences that case *c* has an appreciably earlier potential core break down than case *a* which is due to the enhanced turbulence generation originating from the struts. Furthermore, the comparison of the streamwise profile of the rms fluctuating axial velocity comparison in Fig. 11b shows that the presence of the struts are diminishing the turbulent intensity at the potential core, indicating potentially different sound generation mechanisms for the different jets. Radial profiles of the axial velocity at the nozzle-exit are illustrated in Fig. 12a. An almost constant velocity profile
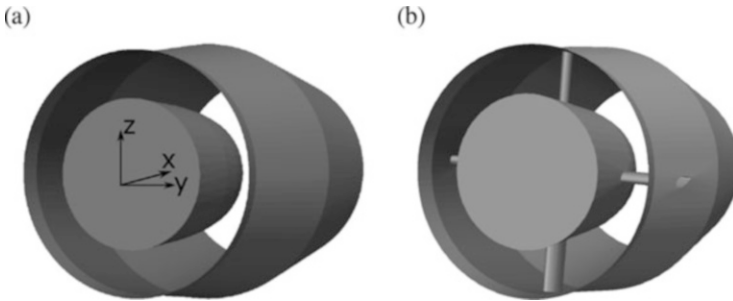

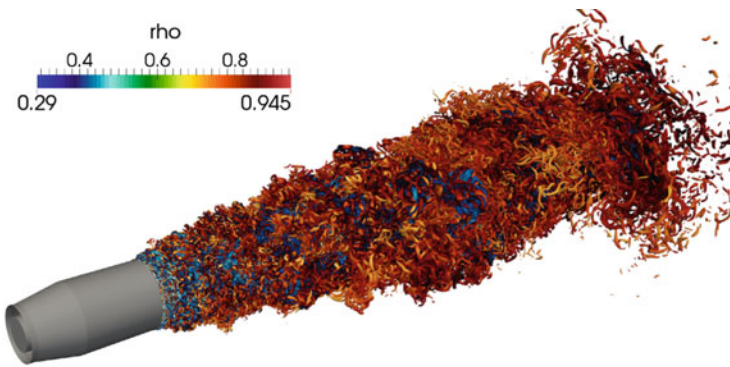**Fig. 9** Nozzle geometries of the (**a**) case *a*, and (**b**) case *c*

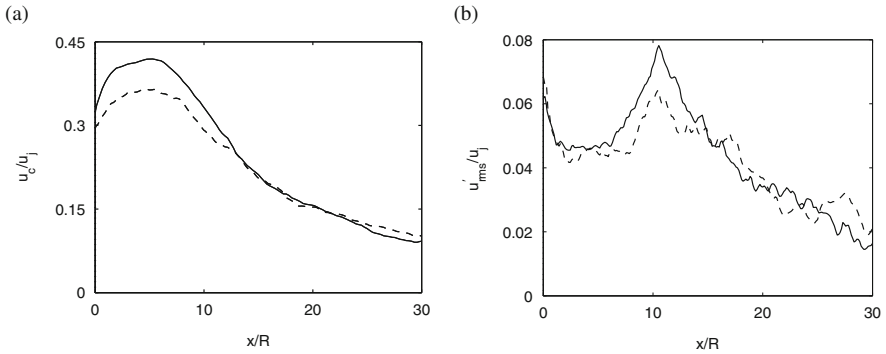**Fig. 10** Perspective view of contours of the Q-criterion color coded with density

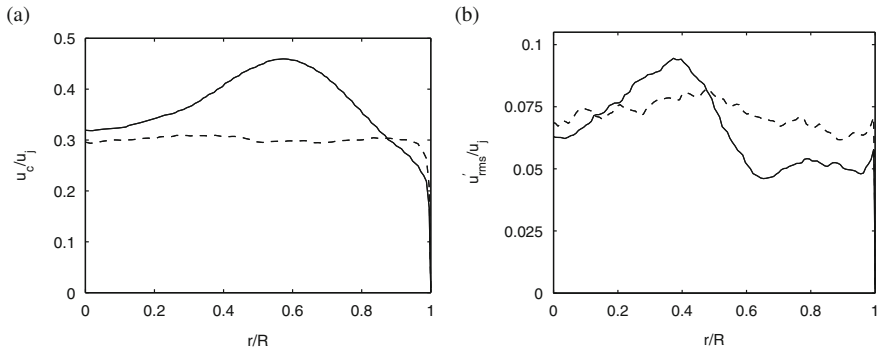**Fig. 11** Streamwise profile of the (**a**) axial velocity, and (**b**) rms fluctuated axial velocity for: (—) case a, (− −) case c

Fig. 12 Nozzle-exit $x/R = 0$ radial profile of the (**a**) axial velocity, and (**b**) rms fluctuated axial velocity for: (—) case a, (− −) case c

for case c is observed. Note that since the nozzle-exit velocity distribution is not axisymmetric, the profile behavior is highly sensitive to the angle of the radius at the nozzle-exit. However, the profile of case a increases for $0 < r/R < 0.6$ and dramatically decreases for $r/R \geq 0.6$. Similarly, case c possesses an almost constant rms fluctuating axial velocity distribution, while case a possesses a velocity deficit for $0.4 < r/R < 0.6$ (see Fig. 12b). A detailed analysis of the geometry effect and non-axisymmetric flow on the jet development is carried out in [21, 22].

5 Axial Fan

In the following section, a rotating axial fan is investigated by LES. The fan configuration has five twisted blades. To reduce the computational costs only one out of five blades is simulated by solving the Navier-Stokes equations in the rotating

frame of reference with periodic boundary conditions in the azimuthal direction as discussed by Pogorelov et. al [23]. First, the sensitivity of the computational results on the grid resolution is analyzed using two different meshes for a fixed operating point defined by the flow coefficient $\phi = \frac{4\dot{V}}{\pi^2 D_o^3 n} = 0.165$. Afterwards, the impact of the flow rate on the flow field with special focus on the tip-gap region is discussed. Therefore, computations at two volume flow rates, i.e., $\phi = 0.165$ and $\phi = 0.195$ are conducted. The diameter of the outer casing wall is $D_o = 300$ mm and the inner diameter of the hub is $D_i = 135$ mm. The rotational speed is $n = 3000$ rpm and the gap between the blade tip and the outer casing wall is $s/D_o = 0.01$ for all computations. The Reynolds number based on the relative velocity of the outer casing wall is $Re = \pi D_o^2 n / \nu = 9.36 \times 10^5$, where ν is the kinematic viscosity.

5.1 Grid Convergence Test

Two different meshes are used for the computations, i.e, case d with 250 million cells and case e with 1 billion cells. Computational resources for both cases are summarized in Table 3. The simulations were conducted on 7992 computing cores for mesh case d and 31,992 computing cores for mesh case e. The time step for both cases is $\Delta t = 1.936 \times 10^{-5} \frac{1}{\pi n}$ and the number of time steps corresponding to four full rotations of the rotor is 0.64×10^6 resulting in a wall clock time of approx. 250 h for each computation. After two full rotations 2000 samples of instantaneous data were collected for statistical analysis.

Figure 13 illustrates a coarse example of the computational grid for the 72° fan section, where Fig. 13a shows the overall computational grid and Fig. 13b highlights the resolution and refinement of the grid in wall regions.

Figure 14 depicts the experimental operating line of the fan showing the pressure coefficient $\Psi = \Delta p/(\frac{\pi^2}{2}\rho D_o^2 n^2)$ as a function of the flow coefficient Φ, where $\Delta p = p_{stat,out} - p_{0,in}$, i.e., the difference of the static pressure at the outlet $p_{stat,out}$ and the stagnation pressure at the inlet $p_{0,in}$ of the fan. As shown, both numerical results agree well with the experimental data.

To give an impression of the overall flow field, Fig. 15a depicts the instantaneous contours of the Q-criterion [20] visualizing the vortical structures. Several physical phenomena are evident, e.g., a development of a passage vortex on the blade root initiating a transition of the incoming boundary layer, a turbulent wake behind the trailing edge of the blade, a transition region on the blades suction side and a jet-like tip-gap vortex due to the leakage flow through the tip-gap generating a turbulent wake region. The flow field inside the tip-gap is caused by the pressure difference

Table 3 Axial fan simulation parameters

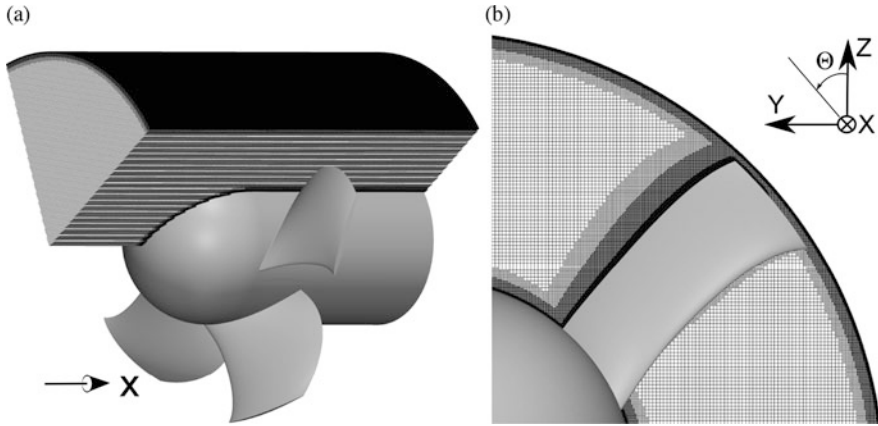|	# cores	Mesh cells	Disc space
Case d	7992	250×10^6	20 TB
Case e	31,992	1000×10^6	80 TB

Fig. 13 Coarse example of the Cartesian mesh resolving one out of five blades of the axial fan; (**a**) axial fan geometry and the overall mesh; (**b**) detailed view of the mesh resolution around the blade
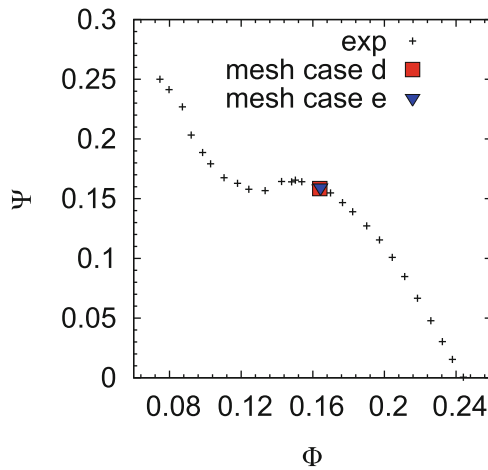

Fig. 14 Operating map for a constant tip-gap size of $s/D_0 = 0.01$ showing the pressure coefficient $\Psi = \frac{\Delta p}{(\frac{\pi^2}{2}\rho D_o^2 n^2)}$, where $\Delta p = p_{stat,out} - p_{0,in}$, i.e., the difference of the static pressure at the outlet $p_{stat,out}$ and the stagnation pressure at the inlet $p_{0,in}$ of the fan, versus the flow coefficient $\Phi = \frac{4\dot{V}}{\pi^2 D_o^3 n}$; experimental data from [24]

between the pressure and the suction side as illustrated by Fig. 15b which shows the instantaneous contours of the pressure coefficient $C_p = \frac{2(p-p_{in})}{\rho(\pi D_o n)^2}$ in the gap region, where p_{in} is the mean inlet pressure. Low pressure regions are observed inside the tip-gap due to separations on the surface of the blade tip and upstream of the blade due to the tip-gap vortex.
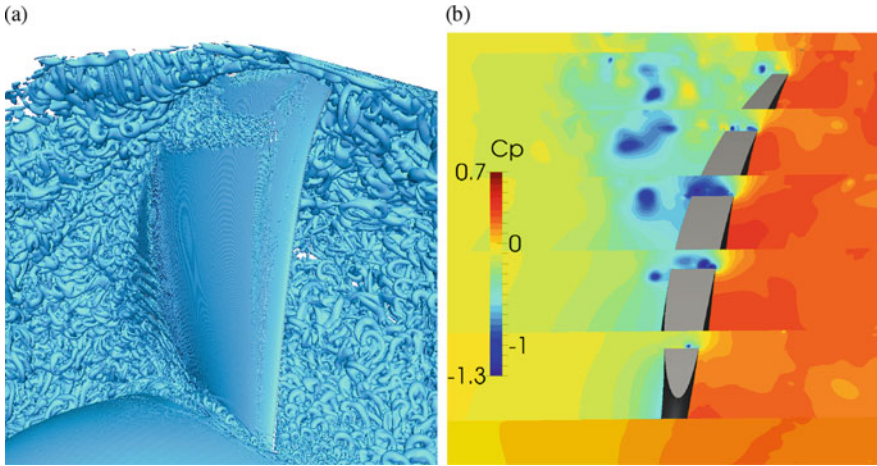
(a)

(b)

Fig. 15 Instantaneous contours of (**a**) the Q-criterion showing the vortical structures around the blade and (**b**) the pressure coefficient showing low pressure regions caused by the tip-gap vortex and the separation vortices inside the tip-gap for mesh case e
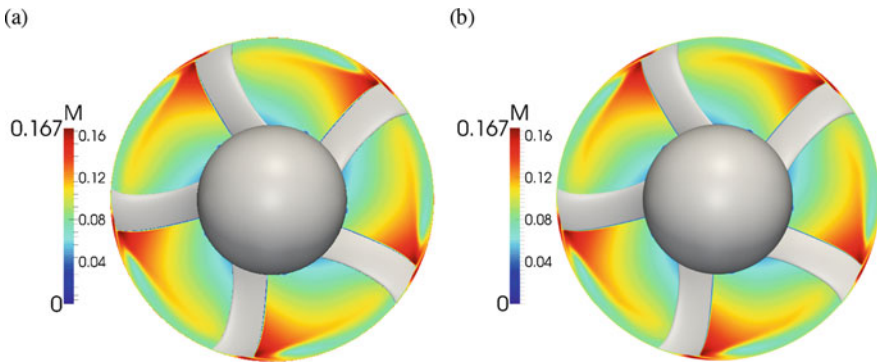
(a)

(b)

Fig. 16 Men relative Mach number contours at a constant axial location $x/D_o = 0.617$; (**a**) mesh case d and (**b**) mesh case e

To analyze the impact of the grid resolution Fig. 16 shows the time-averaged relative Mach number contours at a constant axial location $x/D_o = 0.617$ for mesh case d and e. A marginal impact of the grid resolutions on the Mach number contours in Fig. 16 is observed. For both mesh cases, the Mach number increases in the radial direction and drops in the wake generated by the tip-gap vortex. A maximum Mach number is observed near the tip-gap region.

To further quantify the impact of the mesh, Figs. 17 and 18 show axial distributions of the pressure coefficient and the turbulent kinetic energy at 80 % span and two circumferential locations, i.e., $\Theta = -45°$ and $\Theta = -35°$. Upstream of the blade, the pressure coefficients in Fig. 17 shows a smooth drop due to the suction
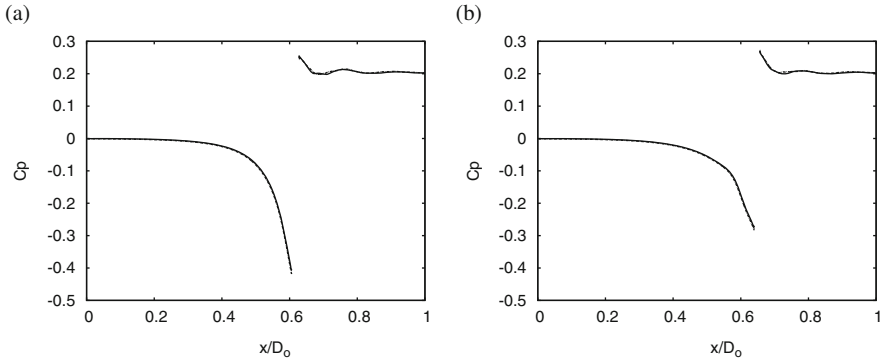
(a)

(b)

Fig. 17 (**a**) Axial distribution of the pressure coefficient at $\Theta = -45°$ and 80 % span; (**b**) Axial distribution of the pressure coefficient at $\Theta = -35°$ and 80 % span; mesh case d (——) , mesh case e (---)
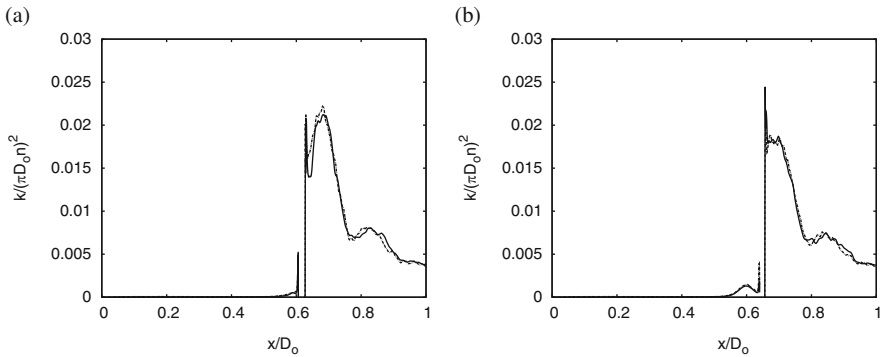
(a)

(b)

Fig. 18 (**a**) Axial distribution of the turbulent kinetic energy at $\Theta = -45°$ and 80 % span; (**b**) Axial distribution of the turbulent kinetic energy at $\Theta = -35°$ and 80 % span; mesh case e (——) , mesh case e (---)

region. Larger values are observed on the pressure side of the blade, as already observed in Fig. 15b. The impact of the mesh on the pressure coefficient is negligibly small and the curves almost perfectly match for both locations. The turbulent kinetic energy distribution in Fig. 18 shows high values on the pressure side of the blade due to the turbulent wake generated by tip-gap vortex of the neighboring blade. Only a small impact of the grid resolution at both location its observed.

5.2 Volume Flow Rate Variation

In this section the impact of the flow coefficient on the flow field near the tip-gap region is demonstrated for mesh case d. Figures 19 and 20 show the time-averaged
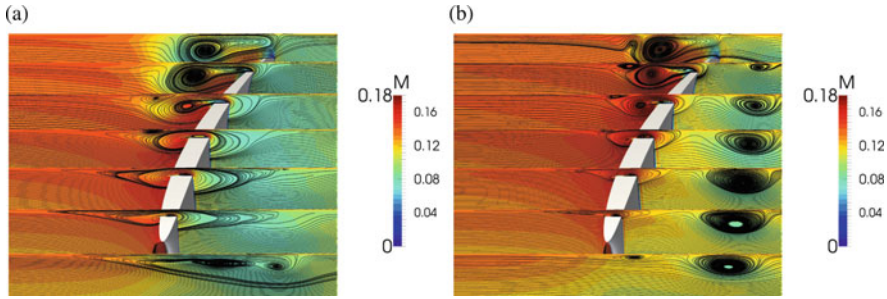
(a)   (b)

Fig. 19 Time-averaged contours of Mach number contours and streamlines of projected velocity vector in different radial planes from $\theta = -30°$ to $\theta = -60°$, for $\phi = 0.165$ (*left*) and $\phi = 0.195$ (*right*). (**a**) $\phi = 0.165$. (**b**) $\phi = 0.195$

(a)   (b)

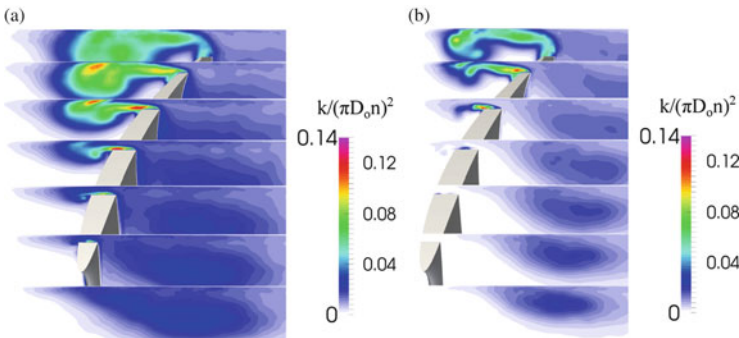**Fig. 20** Turbulent kinetic energy contours in several radial planes from $\theta = -30°$ to $\theta = -60°$, for $\phi = 0.165$ (*left*) and $\phi = 0.195$ (*right*). (**a**) $\phi = 0.165$. (**b**) $\phi = 0.195$

Mach number contours including streamlines of the projected velocity vector and the turbulent kinetic energy contours in several radial planes from $\theta = -30°$ to $\theta = -60°$, for $\phi = 0.165$ and $\phi = 0.195$. For $\phi = 0.195$, the tip-gap vortex passes by the leading edge of the neighboring blade without any interaction. A small counter-rotating separation vortex appears near the leading edge, which, however, has a very low turbulent kinetic energy such that a marginal effect compared to the wake, which impinges upon the blade for the lower volume flow rate, is observed. For $\phi = 0.165$, the tip-gap vortex, which has a larger diameter and is more turbulent, spreads in the axial direction and breaks up in two vortices, where the left vortex is fed by the right vortex and grows. Subsequently, the turbulent left vortex interacts with the leading edge of the blade, which causes strong fluctuations near the gap region extending further upstream compared to $\phi = 0.195$. This results in a larger tip-gap vortex with a higher turbulent kinetic energy, which is created due to the back flow caused by the adverse pressure gradient, supporting the turbulent transition on the suction side. For both volume flow rates, a counter rotating separation vortex is observed next to the tip-gap vortex, which disappears earlier for $\phi = 0.165$.
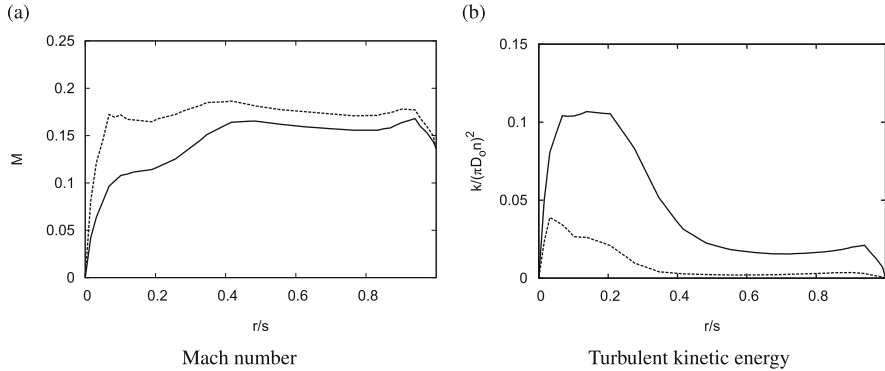
(a)

(b)

Mach number

Turbulent kinetic energy

Fig. 21 Radial distribution of Mach number (**a**) and turbulent kinetic energy (**b**) inside the tip-gap at $x/D_o = 0.617$ and $\theta = -45°$, for $\phi = 0.165$ (—) and $\phi = 0.195$ (−−)

In addition, Fig. 21 depicts the radial distribution of the Mach number and the turbulent kinetic energy inside the tip-gap at $x/D_o = 0.617$ and $\theta = -45°$. The results for $\phi = 0.165$ show a lower Mach number and a higher turbulent kinetic energy inside the tip-gap.

6 Computational Specifications and Scalability Analysis

The simulations were carried out on the CRAY XC40 at HLRS Stuttgart, containing two socket nodes with 12 cores at 2.5 GHz. Each node is equipped with 128 GB of RAM, i.e., each core has 5.33 GB of memory available for the computation. For the scaling experiments a maximum number of grid points for both cases on the order of 1.0×10^9 cells has been used. The scaling test for the fan case has been performed on 228–3828 nodes (i.e., a total number of 5472–91,872 CPUs has been used). For the helicopter engine jet case 418–1668 nodes (10,008–40,032 CPUs) have been used. Details of the scaling experiments for both cases are given in Tables 4 and 5. Up to 183×10^3 cells per domain can be used for the computations owing to the high memory capacity of each nodes. The scaling results are shown in Fig. 22 which indicate a good speed-up for both configurations. Almost the full machine of the

Table 4 Strong scaling speed-up measurements in the fan case

Cores	Cells/domain	Speedup
5472	183×10^3	1.0
10,968	91×10^3	1.87
21,936	45×10^3	3.23
32,880	30×10^3	4.53
91,872	10×10^3	14.49

Table 5 Strong scaling speed-up measurements in the jet case

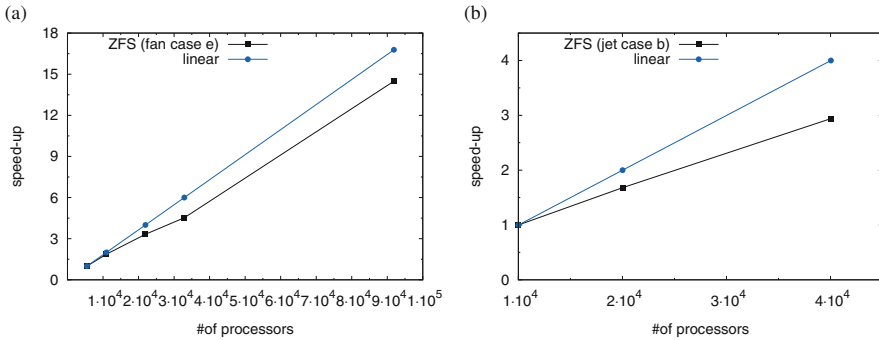| Cores	Cells/domain	Speedup
10,008	100×10^3	1.0
20,016	50×10^3	1.68
40,032	25×10^3	2.94

Fig. 22 Scaling test based on simulations of (**a**) ducted axial fan, and (**b**) helicopter engine jet

Hornet system is used for the fan case, and almost half of the machine is used for the jet case.

7 Conclusion

In this study, LESs simulations have been performed for a helicopter engine jet and a ducted axial fan. To verify the numerical solution method, a coaxial circular hot jet has been computed and the results were compared to reference data. The comparison showed a convincing agreement and hence the applied numerical method can be regarded as reliable. Large-scale computations for a turbulent jet configuration were conducted for a grid convergence test. Hierarchical Cartesian meshes featuring local refinement with a number of cells of 0.329×10^9 and 1.097×10^9 were used. Analogously, a grid dependence study was performed for an axial fan configuration using meshes with a number of cells of 0.25×10^9 and 1×10^9. The analysis showed that $\mathcal{O}(0.3 \times 10^9)$ cells are sufficient to resolve all relevant turbulent structures. Furthermore, computations have been performed for different nozzle geometries, i.e., a simplified nozzle geometry (case a) that consists of a center body and a divergent outer annular channel, and a complete engine nozzle geometry (case c) with 4 additional struts. The presence of the struts results in a different potential core break-down and turbulence intensity at the jet field.

Finally, computations have been performed at two different volume flow rates $\phi = 0.165$ and $\phi = 0.195$ for the axial fan configuration. A periodic boundary condition was used in the azimuthal direction to reduce the computational costs. The smaller volume flow rate results in an interaction of the tip-gap vortex with the

neighboring blade. The interaction leads to a higher turbulent kinetic energy near and inside the tip-gap region.

A code speed-up analysis for the two cases showed a good scalability. For the axial fan configuration almost the complete machine could be used, while for the jet case almost half of the machine was used. For a better understanding of the unsteady flow phenomena, further analysis of the flow field need to be performed. Results of the LES will be used to determine the acoustic field using computational aeroacoustics (CAA) methods in future studies.

References

1. Koh, S.R., Schröder, W., Meinke, M.: Comput. Fluids **78**, 24 (2013)
2. Bogey, C., Bailly, C.: AIAA J. **43**(5), 1000 (2005)
3. Freund, J.B.: J. Fluid Mech. **438**, 277 (2001)
4. You, D., Wang, M., Moin, P.: AIAA Paper 2002-0981 (2002)
5. You, D., Wang, M., Moin, P.: AIAA J. **42**(2), 271–279, (2004)
6. You, D., Wang, M., Moin, P., Mittal, R.: Phys. Fluids **18**(10), 105102 (2006)
7. You, D., Wang, M., Mittal, R., Moin, P.: AIAA Paper 2003-0838 (2003)
8. Boudet, J., Caro, J., Jacob, M.: AIAA Paper 2010-3978 (2010)
9. Boris, J.P., Grinstein, F.F., Oran, E.S., Kolbe, R.L.: Fluid Dyn. Res. **10**(4–6), 199 (1992)
10. Konopka, M., Meinke, M., Schröder, W.: AIAA J. **50**(10), 2102–2114 (2012)
11. Alkishriwi, N., Meinke, M., Schröder, W.: Comput. Fluids **37**(7), 786–792 (2008)
12. Meinke, M., Schröder, W., Krause, E., Rister, T.: Comput. Fluids **31**(4), 695 (2002)
13. Hartmann, D., Meinke, M., Schröder, W.: Comput. Fluids **37**(9), 1103 (2008)
14. Schneiders, L., Hartmann, D., Meinke, M., Schröder, W.: J. Comput. Phys. **235**, 786 (2013)
15. Lintermann, A., Schlimpert, S., Grimmen, J.H., Günther, C., Meinke, M., Schröder, W.: Comput. Methods Appl. Mech. Eng. **277**, 131 (2014)
16. Bogey, C., Bailly, C., Juvé, D.: Theor. Comput. Fluid Dyn. **16**(4), 273 (2003)
17. Pardowitz, B., Tapken, U., Knobloch, K., Bake, F., Bouty, E., Davis, I., Bennett, G.: 20th AIAA/CEAS Aeroacoustics Conference (2014)
18. Kunnen, R.P., Siewert, C., Meinke, M., Schröder, W., Beheng, K.D.: Atmos. Res. **127**, 8–21 (2013)
19. Freund, J.B.: AIAA J. **35**(4), 740–742 (1997)
20. Jeong, J., Hussain, F.: On the identification of a vortex. J. Fluid Mech. **285**, 69–94 (1995)
21. Cetin, M.O., Schröder, W., Meinke, M.: 19th DGLR/STAB Conference (2014)
22. Cetin, M.O., Meinke, M., Schröder, W.: ICWSF Conference (2015)
23. Pogorelov, A., Meinke, M., Schröder, W., Kessler, R.: AIAA Paper 2015-1979 (2015)
24. Zhu, T., Carolus, T.H.: ASME Paper GT2013-94100 (2013)